

# Detection and Correction of Delocalization Errors for Electron and Hole Polarons Using Density-Corrected DFT

Bhaskar Rana,<sup>†</sup> Marc P. Coons,<sup>†</sup> and John M. Herbert\*



Cite This: *J. Phys. Chem. Lett.* 2022, 13, 5275–5284



Read Online

ACCESS |



Metrics & More

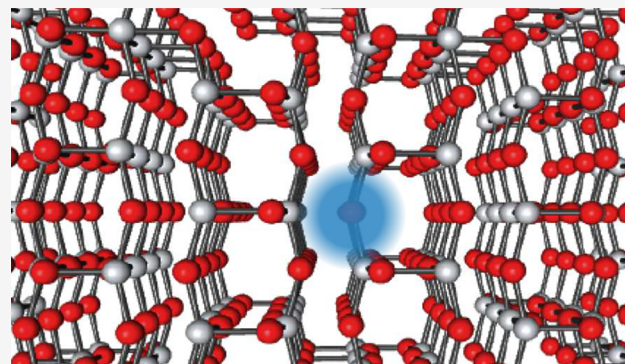


Article Recommendations



Supporting Information

**ABSTRACT:** Modeling polaron defects is an important aspect of computational materials science, but the description of unpaired spins in density functional theory (DFT) often suffers from delocalization error. To diagnose and correct the overdelocalization of spin defects, we report an implementation of density-corrected (DC-)DFT and its analytic energy gradient. In DC-DFT, an exchange-correlation functional is evaluated using a Hartree–Fock density, thus incorporating electron correlation while avoiding self-interaction error. Results for an electron polaron in models of titania and a hole polaron in Al-doped silica demonstrate that geometry optimization with semilocal functionals drives significant structural distortion, including the elongation of several bonds, such that subsequent single-point calculations with hybrid functionals fail to afford a localized defect even in cases where geometry optimization with the hybrid functional does localize the polaron. This has significant implications for traditional workflows in computational materials science, where semilocal functionals are often used for structure relaxation. DC-DFT calculations provide a mechanism to detect situations where delocalization error is likely to affect the results.



One of the most pernicious and long-standing problems in density functional theory (DFT) is that of self-interaction error (SIE),<sup>1–3</sup> which arises from the incomplete cancellation of Hartree self-repulsion by approximate exchange-correlation (XC) functionals. Among the manifestations of SIE is the overstabilization of fractionally charged systems,<sup>4</sup> leading to an underestimation of reaction barrier heights and motivating the use of hybrid functionals.<sup>5,6</sup> When generalized gradient approximations (GGAs) are used to describe open-shell systems, SIE results in exaggerated delocalization of unpaired spins.<sup>7–18</sup> Conventional hybrid functionals with 20–25% exact exchange do not always fully eliminate this “delocalization error”.<sup>17–25</sup> Of particular interest in the present work are polaron defects in transition-metal and main-group oxides, where the extent of defect delocalization is sensitive to the fraction of exact exchange.<sup>20–32</sup> Herein, we demonstrate that density-corrected (DC-)DFT can be used both to detect and to correct the overdelocalization of polaron defects.

DC-DFT is a simple procedure whereby a self-consistent Hartree–Fock (HF) density,  $\rho_{\text{HF}}$ , is used to evaluate the XC energy. This procedure incorporates electron correlation effects but avoids self-consistent iterations at the DFT level, which would introduce SIE into the density, and has been shown to afford reasonable reaction barrier heights even when GGA functionals are used.<sup>33,34</sup> Although this basic idea is an old one,<sup>34–36</sup> it has been revived and championed by Burke

and Sim and their co-workers,<sup>14,37–42</sup> and more recently by others,<sup>43–45</sup> as an *ad hoc* correction for problems where DFT errors are “density-driven” rather than “functional-driven”.<sup>37–41</sup> In such cases, errors may be ameliorated through the use of an SIE-free density, namely,  $\rho_{\text{HF}}$ . The usefulness of DC-DFT therefore hinges on identifying cases where the error is density-driven because otherwise it is probably not advantageous to sacrifice self-consistency.<sup>41,46</sup> Delocalization error in systems with one or more unpaired electrons represents a clear case where the error is density-driven, thus we expect such problems to benefit from DC-DFT.

In the present work, we apply this technique to an electron polaron in  $\text{TiO}_2$  and a hole polaron in doped  $\text{SiO}_2$ . Functional-versus density-driven errors have not previously been considered in these types of systems, yet the open-shell nature of polaron defects suggests that DC-DFT may be advantageous in such cases. (This supposition is supported by results from a density-sensitivity metric,<sup>40</sup> as discussed below.) Within the materials science community there is enormous interest in

Received: April 21, 2022

Accepted: June 3, 2022

polaron transport and trapping in transition-metal oxides,<sup>47–51</sup> yet delocalization error in DFT presents a significant conundrum for the computational modeling of these species.<sup>52</sup>

To introduce the DC-DFT formalism, let us express the energy functional as

$$\tilde{E}[\rho] = T_s[\rho] + v_H[\rho] + v_{\text{ext}}[\rho] + \tilde{E}_{\text{xc}}[\rho] \quad (1)$$

where the tilde indicates that the functional is approximate in practice because of the approximate nature of  $\tilde{E}_{\text{xc}}[\rho]$ , whereas functional forms for the noninteracting kinetic energy ( $T_s$ ), the Hartree potential ( $v_H$ ), and the external potential ( $v_{\text{ext}}$ ) are known. Error in the approximate energy  $\tilde{E}$  may be considered to arise from two contributions:<sup>14</sup> a functional-driven error  $\tilde{E}_{\text{xc}}[\rho] - E_{\text{xc}}[\rho]$  that originates in the approximate nature of the XC functional, where  $\rho$  is the exact density obtained by minimizing the exact functional  $E[\rho]$ , and a density-driven error  $\tilde{E}[\tilde{\rho}] - \tilde{E}[\rho]$ , where  $\tilde{\rho}$  indicates the approximate density obtained by self-consistent variational minimization of eq 1. DC-DFT reduces the density-driven error by eliminating  $\tilde{\rho}$  in favor of  $\rho_{\text{HF}}$ .

The DC-DFT energy expression,  $E_{\text{DC-DFT}} = \tilde{E}[\rho_{\text{HF}}]$ , is not variational and therefore its analytic gradient requires the solution of coupled-perturbed equations.<sup>53,54</sup> Following the formalism in ref 33, the DC-DFT analytic energy gradient is

$$\begin{aligned} \frac{dE_{\text{DC-DFT}}}{dx} &= \frac{\partial E_{\text{DC-DFT}}}{\partial x} + \sum_{\mu\nu} \frac{\partial E_{\text{DC-DFT}}}{\partial P_{\mu\nu}} \frac{\partial P_{\mu\nu}}{\partial x} \\ &= \frac{\partial E_{\text{DC-DFT}}}{\partial x} + \sum_{\mu\nu} F_{\mu\nu}^{\text{KS}} \frac{\partial P_{\mu\nu}}{\partial x} \end{aligned} \quad (2)$$

where  $P_{\mu\nu}$  is the HF density matrix and  $F_{\mu\nu}^{\text{KS}}$  is the Kohn–Sham (KS) Fock matrix constructed from it. Operationally, derivatives  $\partial P_{\mu\nu}/\partial x$  are obtained from molecular orbital (MO) coefficient derivatives,<sup>54</sup> solving the coupled-perturbed equations in Z-vector form for efficiency.<sup>53</sup> This is similar to the procedure used for the DFT Hessian, which requires  $\partial P_{\mu\nu}/\partial x$  even in a fully self-consistent treatment.<sup>54–56</sup> Although the DC-DFT energy is not variational, its gradient is certainly not “ill-defined” as some have claimed.<sup>57</sup> Molecular properties such as multipole moments, polarizabilities, infrared and Raman intensities, and magnetic resonance parameters can each be cast in the form of energy derivatives,<sup>58</sup> and these properties are also well-defined in DC-DFT.

DC-DFT and its analytic gradient have been implemented in the Q-Chem program<sup>59</sup> and will be available in Q-Chem v. 6.0. Validation tests are described in the Supporting Information, including comparisons between analytic and finite-difference gradients (Tables S1–S4) and a demonstration that DC-DFT conserves energy in an *ab initio* molecular dynamics simulation (Figure S1). We also reproduced previous results<sup>33</sup> demonstrating that DC-BLYP affords improved reaction barriers as compared to either self-consistent BLYP or HF calculations (Table S5).

The remainder of this work describes the application of DC-DFT to polaron defects in oxide materials, where GGAs exhibit significant delocalization error. Periodic DFT is typically the method of choice for modeling solid-state materials but that approach has failed to reproduce correct ground-state electronic and geometric structure in important cases,<sup>25–27,60–63</sup> particularly with respect to the localized nature of O(2p)-derived holes obtained in doped silica and metal oxides. One such example is the polaron in Al-doped

silica ( $\text{SiO}_2$ ),<sup>24–28,62</sup> where a  $\text{Si}^{4+}$  ion is replaced by  $\text{Al}^{3+}$ . Electron paramagnetic resonance (EPR) spectroscopy suggests that the unpaired spin is localized on a single oxygen atom adjacent to the defect center,<sup>64–66</sup> creating a local structural distortion with a single elongated Al–O bond.

This picture is reproduced by unrestricted HF calculations using cluster models, which indicate that the hole localizes onto a single defect-adjacent oxygen atom.<sup>22–27</sup> Hyperfine coupling parameters for  $^{17}\text{O}$ ,  $^{29}\text{Si}$ , and  $^{27}\text{Al}$  are consistent with experiment when computed at the HF level,<sup>25–27</sup> or alternatively using DFT with a large fraction of exact exchange,<sup>24</sup> and the defect exhibits local symmetry breaking and Jahn–Teller reconstruction.<sup>26</sup> Application of semilocal functionals to cluster models, however, affords a hole that is delocalized over all four neighboring oxygen atoms at the Al center, without significant structural distortion.<sup>27,60</sup> A localized defect is recovered by applying a self-interaction correction,<sup>28</sup> or by using functionals with a large fraction of exact exchange.<sup>24,26</sup> Notably, B3LYP (with 20% exact exchange) fails to localize the hole in Al-doped  $\text{SiO}_2$ ,<sup>24–26</sup> whereas the functional BB1K (with 42% exact exchange) does localize it,<sup>22,26</sup> as does DFT+*U* with a large Hubbard *U* parameter.<sup>62</sup>

Using the cluster models shown in Figure 1, which are similar to those used in ref 27, we have investigated whether

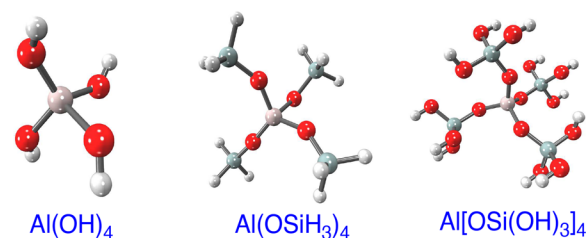


**Figure 1.** Cluster models of Al-doped silica, where the central Si atom of the  $\text{SiO}_2$  crystal structure is replaced by Al, which is the central atom in each cluster.

DC-DFT is beneficial in describing the localization of the hole in Al-doped silica. We created defects by replacing the central Si atom with Al and capping the terminal oxygen atoms with hydrogen so that the clusters are charge neutral. All three structures in Figure 1 were initially optimized using second-order Møller–Plesset perturbation theory (MP2), with the 6-31G\* basis set within the resolution-of-identity approximation.

DC-DFT is advantageous only if the density-driven error is large,<sup>38–41</sup> so we examine that question first. A metric

$$S = |\tilde{E}[\rho_{\text{LDA}}] - \tilde{E}[\rho_{\text{HF}}]| \quad (3)$$

has been suggested to quantify the density sensitivity of a given functional  $\tilde{E}[\rho]$ .<sup>39–41</sup> In eq 3, this approximate functional is evaluated using the self-consistent density obtained either from a HF calculation or else from the local density approximation (LDA). For small molecules and clusters, values  $S > 2$  kcal/mol have been suggested as cases where DC-DFT may improve the results.<sup>40,41</sup> For the structures in Figure 1, values of  $S$  computed using either PBE or BLYP are much larger than this threshold, e.g.,  $S > 30$  kcal/mol for  $\text{Al}(\text{OH})_4$  and  $S > 120$  kcal/mol for  $\text{Al}[\text{OSi}(\text{OH})_3]_4$  (Table S6). This indicates sizable density sensitivity but also suggests that the metric  $S$  may increase with system size, at least until the system is large enough for delocalization to reach its asymptotic limit. As such, we also compute  $S/N_{\text{atoms}}$  as a metric that is more similar

across cluster sizes. This quantity ranges from 2.6 to 7.5 kcal/mol for the three Al-doped silica models that we consider (Table S6). We suggest that the normalized metric  $S/N_{\text{atoms}}$  is a more general alternative to  $S$  that should be used going forward.

Consistent with experiment, MP2 optimization affords a localized hole (Figure 2a) and a single elongated Al–O bond

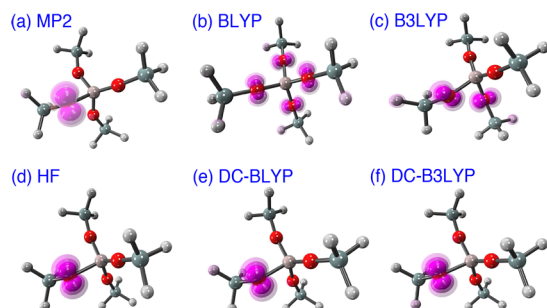


**Figure 2.** Spin densities for  $\text{Al}(\text{OSiH}_3)_4$  using geometries that have been optimized at the indicated levels of theory. For DC-BLYP and DC-B3LYP, the HF spin density is plotted, and for MP2 we plot the “relaxed” (correlated) one-electron spin density. Spin densities computed at PBE- and PBE0-optimized structures are not shown because they are essentially indistinguishable from the BLYP and B3LYP results, respectively. The 6-31G\* basis is used for MP2 and 6-31++G\* is used for the other methods.

length (Table 1). Starting from the MP2-optimized structure for each cluster, we next performed geometry optimizations at various DFT levels of theory to investigate the structural distortion and (de)localization of the hole. As indicators of distortion, Al–O bond lengths around the defect center are listed in Table 1 for several different functionals and their DC-DFT analogues. Spin densities ( $\rho_\alpha - \rho_\beta$ ) for the  $\text{Al}(\text{OSiH}_3)_4$  cluster are shown in Figure 2, and those for the other clusters are shown in Figures S2 and S3.

Cluster structures optimized at the SIE-free HF and MP2 levels of theory exhibit a single elongated Al–O bond, whereas the remaining three Al–O bonds have nearly identical bond lengths. In contrast, geometries obtained with GGA functionals (BLYP and PBE) exhibit four identical Al–O bond lengths and very little structural distortion. This is consistent with a hole that is delocalized over all four bonds, as shown for BLYP in

Figure 2b, but is inconsistent with EPR spectroscopy. For hybrid functionals PBE0 and B3LYP, the hole is delocalized over two Al–O bonds rather than four (Figure 2c). This is reflected in two elongated Al–O bonds whose bond lengths have intermediate values between the short and long Al–O bond lengths obtained at the MP2 level (Table 1).

For the hybrid functionals, Al–O distances are omitted from Table 1 for the largest cluster,  $\text{Al}[\text{OSi}(\text{OH})_3]_4$ , because the hole migrates to the surface of the cluster as the geometry is relaxed, ultimately delocalizing over the surface oxygen atoms around the Si centers (Figure S3). Even hybrid functionals PBE0 and B3LYP thus fail qualitatively in their description of the hole polaron in this system, consistent with previous results.<sup>24–26</sup>

In contrast, upon relaxing the structure of each doped silica cluster using DC-DFT, starting from the localized MP2 structure, localization is preserved in all cases: DC-BLYP (Figure 2e), DC-B3LYP (Figure 2f), DC-PBE, and DC-PBE0. (Note that the DC-DFT spin densities in Figure 2 are HF densities because plotting DFT spin densities would be inconsistent with the strategy of DC-DFT, which is to avoid introducing SIE by avoiding the DFT density altogether.) Consistent with the localized spin densities obtained with DC-DFT, the bond lengths in Table 1 show that all four DC-DFT methods afford a single elongated Al–O bond, with bond lengths that are within 0.03 Å (or less) of MP2 results, for both the shorter and longer Al–O bonds.

DC-DFT geometry optimizations afford a properly localized hole in these doped silica clusters precisely because the energy and gradient avoid the use of a DFT density. To emphasize this point, Table 2 reports Mulliken “spin charges” (obtained from  $\rho_\alpha - \rho_\beta$ ) for the oxygen atoms around the Al defect, computed using either the HF density or else the BLYP density, at the same optimized geometry of the cluster in either case. For the DC-DFT cases in Table 2, this means that we perform the geometry optimization using  $\rho_{\text{HF}}$  but then evaluate  $\rho_{\text{BLYP}}$  at the optimized geometry, for demonstrative purposes. (Results based on  $\rho_{\text{HF}}$  represent the proper DC-DFT procedure.) Despite the limitations of the Mulliken procedure, these spin charges have proven to be an effective way to characterize the (de)localization of a radical center,<sup>16–18</sup> and a similar picture is obtained with the larger def2-TZVPD basis set (Table S8).

**Table 1.** Optimized Al–O Bond Distances (in Å) in Al-Doped Silica Models

model	bond	geometry optimization method									
		HF	MP2	BLYP	PBE	B3LYP	PBE0	DC-BLYP	DC-PBE	DC-B3LYP	DC-PBE0
$\text{Al}(\text{OH})_4$	Al–O <sub>1</sub>	2.07	2.09	1.80	1.79	1.84	1.84	2.09	2.08	2.07	2.06
	Al–O <sub>2</sub>	1.71	1.73	1.78	1.78	1.72	1.72	1.73	1.73	1.72	1.71
	Al–O <sub>3</sub>	1.72	1.75	1.78	1.78	1.72	1.71	1.75	1.75	1.74	1.74
	Al–O <sub>4</sub>	1.71	1.73	1.79	1.78	1.84	1.84	1.73	1.73	1.72	1.71
$\text{Al}(\text{OSiH}_3)_4$	Al–O <sub>1</sub>	1.70	1.73	1.76	1.76	1.81	1.81	1.72	1.72	1.71	1.71
	Al–O <sub>2</sub>	1.70	1.73	1.76	1.76	1.71	1.70	1.72	1.72	1.71	1.71
	Al–O <sub>3</sub>	1.69	1.71	1.76	1.76	1.71	1.70	1.71	1.71	1.70	1.70
	Al–O <sub>4</sub>	2.00	1.99	1.76	1.76	1.81	1.81	2.01	1.99	1.99	1.98
$\text{Al}[\text{OSi}(\text{OH})_3]_4$	Al–O <sub>1</sub>	1.94	1.94	1.79	1.78	<sup>a</sup>	<sup>a</sup>	1.97	1.93	1.95	1.92
	Al–O <sub>2</sub>	1.72	1.76	1.78	1.78	<sup>a</sup>	<sup>a</sup>	1.75	1.75	1.74	1.73
	Al–O <sub>3</sub>	1.71	1.74	1.73	1.73	<sup>a</sup>	<sup>a</sup>	1.71	1.74	1.71	1.72
	Al–O <sub>4</sub>	1.71	1.73	1.78	1.78	<sup>a</sup>	<sup>a</sup>	1.73	1.73	1.72	1.72

<sup>a</sup>Spin delocalization moves the defect toward the surface oxygen atoms (Figure S3).

Table 2. Mulliken Spin Charges<sup>a</sup> (in a.u.) around the Al Dopant in Silica Clusters<sup>b</sup>

complex	geometry	HF density				BLYP density			
		O <sub>1</sub>	O <sub>2</sub>	O <sub>3</sub>	O <sub>4</sub>	O <sub>1</sub>	O <sub>2</sub>	O <sub>3</sub>	O <sub>4</sub>
Al(OSiH <sub>3</sub> ) <sub>4</sub>	HF	0.01	0.01	-0.01	1.02	0.11	0.11	0.05	0.57
	BLYP	0.25	0.24	0.25	0.25	0.19	0.19	0.19	0.19
	PBE	0.24	0.24	0.25	0.25	0.19	0.19	0.19	0.19
	B3LYP	0.47	-0.00	-0.00	0.50	0.40	0.03	0.03	0.40
	PBE0	0.49	-0.00	-0.00	0.49	0.43	0.01	0.01	0.43
	DC-BLYP	0.01	0.00	-0.01	1.02	0.13	0.09	0.05	0.57
	DC-PBE	0.01	0.01	-0.01	1.02	0.12	0.11	0.04	0.57
	DC-B3LYP	0.00	0.01	-0.01	1.02	0.10	0.13	0.04	0.57
Al[OSi(OH) <sub>3</sub> ] <sub>4</sub> <sup>c</sup>	DC-PBE0	0.01	0.01	-0.01	1.02	0.12	0.11	0.04	0.57
	HF	0.99	-0.01	0.01	0.00	0.69	0.00	0.05	0.05
	DC-BLYP	1.02	-0.01	-0.01	0.01	0.64	0.01	0.03	0.11
	DC-PBE	0.99	0.00	0.00	0.00	0.67	-0.00	0.02	0.06
	DC-B3LYP	1.01	-0.01	-0.00	0.01	0.64	0.01	0.03	0.11
	DC-PBE0	0.98	-0.01	0.00	0.00	0.67	0.00	0.02	0.05

<sup>a</sup>6-31++G\* basis set. <sup>b</sup>See Table S7 for Al(OH)<sub>4</sub>. <sup>c</sup>Data for PBE, BLYP, PBE0, and B3LYP are not shown because of significant delocalization (Figure S3).

Whereas DC-DFT affords a well-localized hole with a single spin charge of  $\approx 1$ , the BLYP density evaluated at the same geometry reintroduces delocalization of the hole, reducing the spin charge to  $\approx 0.7$  in Al(OH)<sub>4</sub> and to  $\approx 0.6$  in Al(OSiH<sub>3</sub>)<sub>4</sub>. The hole does not completely delocalize because the HF- or DC-DFT-optimized geometry elongates one Al–O bond, creating a bond dipole that is evidently sufficient to partially localize the spin density even in BLYP or PBE calculations. When one of those GGA functionals is used to optimize the geometry, however, delocalization becomes complete and results in four equivalent spin charges on the oxygen atoms surrounding the Al defect. For the largest cluster, Al[OSi(OH)<sub>3</sub>]<sub>4</sub>, GGA calculations at GGA-optimized geometries afford a hole that is completely delocalized over the entire cluster. Conversely, geometries optimized using either B3LYP or PBE0 result in two elongated Al–O bonds. In these cases, the two exaggerated bond dipoles are large enough that a subsequent HF calculation cannot completely localize the hole, and instead two significant spin charges are obtained, with values of  $\approx 0.6$  in Al(OH)<sub>4</sub> and  $\approx 0.5$  in Al(OSiH<sub>3</sub>)<sub>4</sub>.

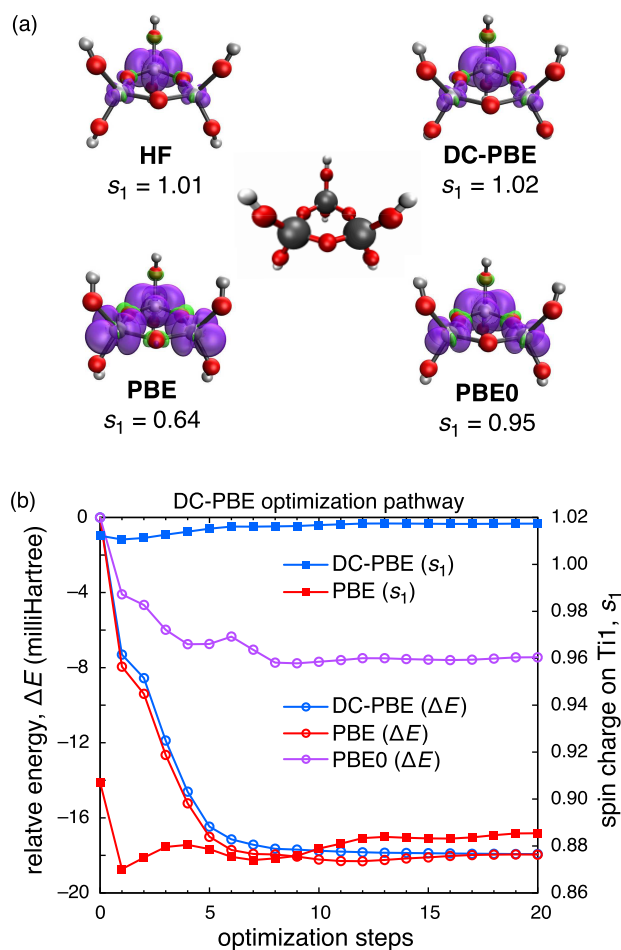
Whereas calculations reported up to this point use a dopant to create a hole, in transition-metal oxides it is possible to create localized electronic states via structural distortion following excitation at the band gap,<sup>50,51,67,68</sup> with important applications in photocatalysis.<sup>69,70</sup> For simplicity, we create electron polarons in the ground state of model systems representing titania by introducing an extra electron into a closed-shell system, and we find that many of the same trends are on display as were observed with dopant-induced holes. For example, consider the small (TiO<sub>2</sub>)<sub>3</sub>(H<sub>2</sub>O)<sub>3</sub> cluster that is depicted in Figure 3a. By breaking the symmetry of the ring and introducing an unpaired electron, a spin-localized structure for [(TiO<sub>2</sub>)<sub>3</sub>(H<sub>2</sub>O)<sub>3</sub>]<sup>-</sup> can be optimized at the HF level, and this localization is preserved upon structural relaxation using DC-PBE (Figure 3a). Relaxation at the PBE level, however, leads to significant spin delocalization, with Mulliken spin charges  $s_1 = 0.64$  and  $s_2 = 0.24 = s_3$  on the three Ti atoms. PBE0 optimization leads to a much smaller amount of delocalization ( $s_1 = 0.95$  and  $s_2 = 0.07 = s_3$ ).

Figure 3b examines the energetics with various approaches, computed along the DC-PBE geometry optimization pathway starting from the spin-localized HF structure. Nearly identical

energetics to those obtained at the DC-PBE level (used to optimize the structure) are obtained when the energy is evaluated at each step along the pathway using a self-consistent PBE calculation. Furthermore, the spin remains largely localized on a single Ti atom despite the fact that a self-consistent PBE geometry optimization produces a much more delocalized electronic structure. This suggests that SIE drives geometric distortions that, in turn, facilitate additional delocalization, creating a feedback loop when the GGA functional is employed self-consistently.

We will investigate this further using larger models of anatase TiO<sub>2</sub>, an important material in photocatalytic and photovoltaic applications.<sup>69–72</sup> Understanding the behavior of polaronic states is crucial in understanding charge transport in this and other metal oxide photocatalysts,<sup>47–52</sup> but the degree to which an electron polaron localizes in anatase TiO<sub>2</sub> has been a subject of debate. Some studies predict delocalization of the excess charge over multiple Ti ions,<sup>73–75</sup> while others suggest the formation of a localized or “self-trapped” polaron.<sup>68</sup> It has been suggested that localized and delocalized states may be similar in energy,<sup>76</sup> and that the localization properties may vary from one crystal polymorph to another.<sup>74</sup> Semilocal functionals overstabilize charge-delocalized structures,<sup>29</sup> and while this propensity is somewhat reduced by employing hybrid functionals,<sup>30,31</sup> or alternatively via DFT+*U*,<sup>75–80</sup> the use of potentially nontransferrable parameters (such as the fraction of exact exchange or the Hubbard *U* parameter) means that some experimental data are needed to determine the correct approach.<sup>77</sup> However, EPR experiments have produced conflicting evidence regarding the (de)localization of electron polarons in anatase TiO<sub>2</sub>.<sup>73</sup>

We constructed a cluster model of anatase TiO<sub>2</sub> as follows. Starting from the crystal structure of the bulk material, we extracted a cluster Ti<sub>21</sub>O<sub>70</sub>H<sub>56</sub> that is depicted in Figure 4a, capping the surface oxygen atoms with hydrogen to maintain charge neutrality. This has been suggested to be the smallest cluster model where the central Ti atom retains bulk TiO<sub>2</sub> character.<sup>81</sup> The geometry of this cluster model was then relaxed using HF theory but constraining the surface Ti–O and O–H bond lengths to provide some mechanical stability at the surface. Following ref 81, these optimizations used the



**Figure 3.** (a) Spin densities for  $[(\text{TiO}_2)_3(\text{H}_2\text{O})_3]^-$ , with positive and negative values of  $\rho_\alpha - \rho_\beta$  indicated in purple and green, respectively. The central structure emphasizes the Ti atoms as larger gray spheres, and around the periphery are structures optimized at the indicated levels of theory. (The LANL2DZ basis set and pseudopotential are used in each case.) The quantity  $s_1$  is the Mulliken spin charge on the Ti atom at the apex of the ring. (b) Relative energies  $\Delta E$  (open circles, to be read from the scale on the left) and spin charges  $s_1$  (filled squares, scale on the right) along the DC-PBE relaxation pathway starting from the HF-optimized structure.

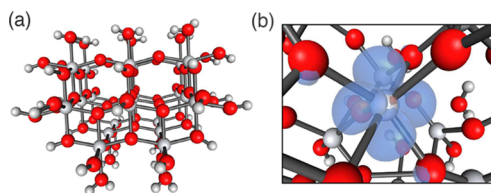


**Figure 4.** Cluster model of an electron polaron in anatase  $\text{TiO}_2$ . (a) Capped cluster  $\text{Ti}_{21}\text{O}_{70}\text{H}_{56}$  extracted from the bulk  $\text{TiO}_2$  crystal structure. (b) HF spin density for a localized polaron in  $[\text{Ti}_{21}\text{O}_{70}\text{H}_{56}]^-$ .

LANL2DZ basis set along with the eponymous effective core potential for Ti.<sup>82</sup>

A model for an electron polaron is obtained by adding an extra electron to the  $\text{Ti}_{21}\text{O}_{70}\text{H}_{56}$  cluster model in a manner such that the polaron is associated with the central (bulk-like) Ti atom. Naive approaches to adding this electron cause it to delocalize at the surface of the cluster, which is an edge effect rather than an SIE artifact, as evidenced by problematic

delocalization even at the HF level. Various strategies have been devised to obtain a localized polaron in a finite cluster model,<sup>83</sup> typically involving either bond distortion or else changes to the nuclear charges. Following other theoretical studies of  $\text{TiO}_2$ , in which Ti–O bond lengths were elongated by 2–8% in order to localize the defect,<sup>31,84</sup> we opted to elongate all six Ti–O bonds around the central Ti atom in the initial geometry of  $[\text{Ti}_{21}\text{O}_{70}\text{H}_{56}]^-$ . The elongated Ti–O bond lengths at the initial geometry can be seen in Figure S4c, and the structure was subsequently relaxed at the HF level using the Mulliken spin charge  $s(\text{Ti}^*)$  on the central atom ( $\text{Ti}^*$ ) to monitor (de)localization as the optimization proceeds. This analysis demonstrates that the localized polaron that is initially induced by bond elongation remains localized when the structure is relaxed at the HF level (Figure 4b). The density sensitivity at the HF-optimized polaron geometry is  $S/N_{\text{atoms}} \approx 8$  kcal/mol using either BLYP or PBE, which is even larger than was found for the Al-doped silica clusters.

Spin charges computed at the PBE0 level along the HF optimization trajectory (Figure S4b) also correspond to a localized defect. In contrast, the PBE functional partially delocalizes the polaron even when the HF structure is used, with  $s(\text{Ti}^*) < 0.6$  at the HF-optimized geometry as compared to values  $s(\text{Ti}^*) \approx 1$  that are obtained using either HF or PBE0. This is the same behavior that was observed for Al-doped silica. In the HF-optimized structure of  $[\text{Ti}_{21}\text{O}_{70}\text{H}_{56}]^-$ , all of the  $\text{Ti}^*-\text{O}$  bonds are longer than their values in the neutral structure, but two of them exhibit significantly greater elongation, suggesting the participation of two Ti–O bonds (Figure S4c).

We next investigate whether this level of localization persists with DFT. Starting from the HF-optimized structure of  $[\text{Ti}_{21}\text{O}_{70}\text{H}_{56}]^-$ , we reoptimized the geometry using either PBE or PBE0 and monitored  $s(\text{Ti}^*)$  as a proxy for polaron localization. The results are plotted in Figure 5. Bond-length analysis along the PBE0 optimization pathway (Figure S5a) suggests a localized polaron, and a plot of  $s(\text{Ti}^*)$  along the same pathway (Figure 5a) demonstrates that the extra electron indeed remains localized on the central atom,  $\text{Ti}^*$ . If  $s(\text{Ti}^*)$  is computed instead using the PBE functional, along the same PBE0 optimization pathway, then the polaron seems stable but a significant fraction of the spin density is transferred onto other atoms, resulting in  $s(\text{Ti}^*) < 0.6$ .

When the optimization is performed instead with PBE, then not only is the PBE polaron significantly delocalized, with  $s(\text{Ti}^*) < 0.2$ , but also the spin charge computed using PBE0 indicates that PBE-driven changes in bond lengths cause delocalization that persists at the PBE0 level. The value of  $s(\text{Ti}^*)$  starts at  $\approx 1$  when computed with PBE0 but falls to  $< 0.5$  along the PBE optimization pathway, with significant fluctuations in between (Figure 5b). When the HF density is evaluated along this PBE optimization pathway, Mulliken charges indicate hopping of the polaron between Ti atoms. This behavior likely arises from a combination of HF theory's strong tendency to localize charge, combined with a GGA optimization that is driving the elongation of multiple Ti–O bonds. At any given step along the pathway, the HF calculation localizes the polaron on whichever Ti–O bond is longest, and that location switches several times over the course of the optimization (Figure 5Sb).

These observations are significant in view of a standard operating procedure in computational materials science, which is to perform geometry optimizations using GGA functionals

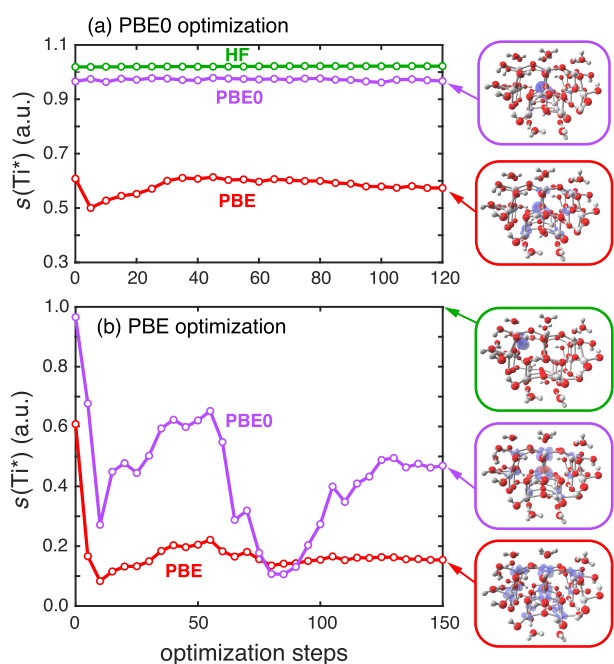


**Figure 5.** Variation of the spin charge  $s$  on the central Ti atom ( $\text{Ti}^*$ ) in  $[\text{Ti}_{21}\text{O}_{70}\text{H}_{36}]^-$ , computed at different levels of theory as the structure is optimized using (a) PBE0 versus (b) PBE. The starting structure in either case is optimized at the HF level and exhibits a localized polaron. Insets on the right show the spin densities at various ending points. In (b), the HF result for  $s(\text{Ti}^*)$  is not shown because the spin density hops between being localized on different Ti atoms as the optimization proceeds.

and then to use hybrid functionals for single-point energy calculations at GGA-optimized geometries. (This procedure mitigates the high cost of hybrid DFT under periodic boundary conditions.) Our results demonstrate that PBE optimization drives the system into structures that are severely affected by SIE, with elongated bonds (consistent with a fully delocalized spin defect) from which a PBE0 single-point calculation cannot recover. A PBE0 calculation at the PBE-optimized geometry thus affords a delocalized polaron, which

is a qualitatively different result as compared to what is obtained when PBE0 is used for the optimization.

We next evaluate the performance of DC-DFT along the PBE and PBE0 optimization pathways. The PBE pathway is more interesting insofar as a major change in polaron localization is observed in this case, as evident from the spin charges in Figure 5b. We seek to assess the extent to which this density-driven error is mitigated by DC-DFT. This assessment requires a benchmark that is SIE-free, for which we choose MP2/def2-SVP. The treatment of dynamical correlation may help to assuage a tendency toward overlocalization that is exhibited by the HF method, which is evident from its behavior for fractional electron systems.<sup>85</sup> MP2 is not always a good choice for transition-metal systems, but the closed-shell nature of the  $\text{Ti}^{4+}$  ions makes it acceptable here, and MP2 has been used to provide benchmarks for  $\text{TiO}_2$  clusters.<sup>86–90</sup>

Figure 6 reports the results of single-point energy calculations along the PBE and PBE0 optimization pathways. The starting point is a HF-optimized structure, hence the HF energy immediately rises as either a PBE- or PBE0-driven optimization moves the system away from the minimum-energy HF geometry. Notable discontinuities in the HF energy along the PBE pathway (Figure 6a) arise when the localized HF polaron jumps between Ti centers, as a result of HF theory's strong tendency to localize unpaired spins, combined with the simultaneous distortion of numerous Ti–O bonds due to PBE delocalization error. In Figure S8, one can observe that the HF polaron is localized on a different Ti atom in the starting and ending structures optimized at the PBE level. Jumps in the HF energy in Figure 6a correlate with jumps in the gap between the highest occupied molecular orbital (HOMO) and the lowest unoccupied molecular orbital (LUMO), computed at the HF level (Figure S9a). These gaps are absent at the PBE level, consistent with the well-known band gap problem associated with GGA functionals,<sup>91–93</sup> which reflects the absence of a proper derivative discontinuity and is thus intimately connected to SIE and delocalization error.<sup>92</sup> A Born–Oppenheimer molecular dynamics simulation using a GGA functional might therefore be anticipated to afford incorrect polaron dynamics because

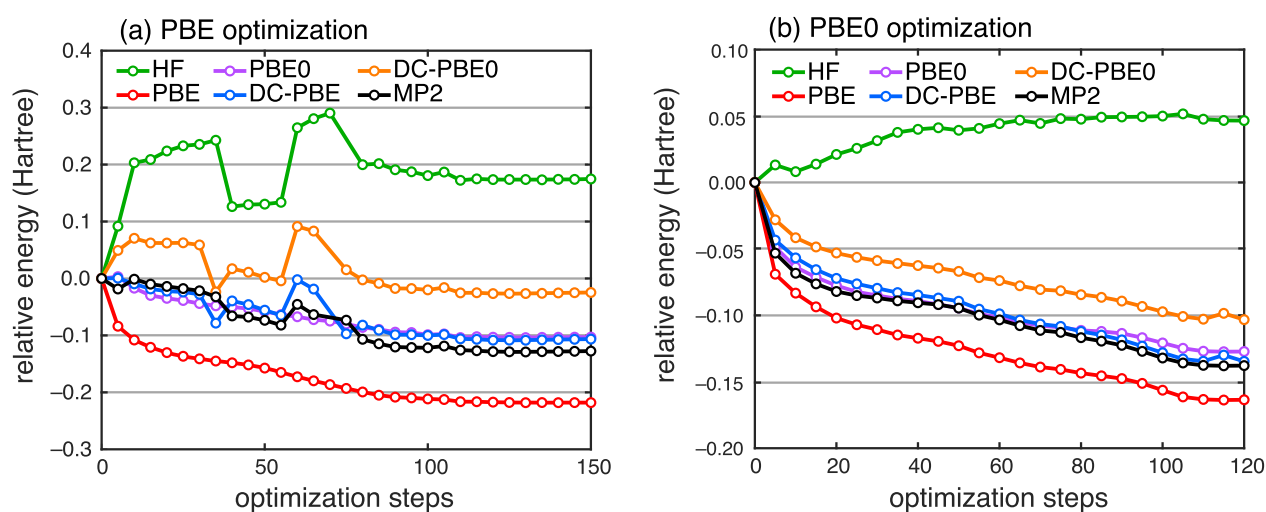


**Figure 6.** Relative energies along (a) PBE and (b) PBE0 optimization pathways for an electron polaron in anatase  $\text{TiO}_2$ , starting from a HF-optimized geometry that localizes the polaron on the central Ti atom. Single-point energy calculations (def2-SVP basis) are performed using each of the methods indicated. All energies are shifted to a common value at the initial structure.

changes in the electronic configuration are rendered thermally accessible by artificially small energy gaps.

Even a modest fraction of exact exchange introduces something of a derivative discontinuity, and the energetics at the PBE0 level of theory closely track the MP2 results. The MP2, hybrid DFT, and DC-DFT methods do inherit jumps in energy when the polaron localizes on a different site, although MP2 substantially mutes this effect as compared to HF theory. These jumps are essentially artifacts of the GGA-driven optimization and are absent when either PBE0 or HSE06 is used to optimize the geometry (Figures 6b and S10a, respectively). Note also that in the latter two cases the PBE functional lowers the energy even faster than the hybrid functional that is being used to optimize the geometry! This is an SIE artifact (overstabilization of fractional charges), and PBE predicts a delocalized polaron even at the PBE0-optimized geometry, where PBE0 itself localizes the polaron (Figure 5a). Overall, the close match between PBE0 and MP2 suggests that the former is a good level of theory for this system, although that fact is evident only in light of the MP2 results.

When DC-DFT is applied to this system, energetics for the PBE optimization pathway are shifted upward by about 0.1 hartree, placing DC-PBE in reasonable agreement with MP2. The same is true for DC-PBE along the PBE0 optimization pathway, only in that case the DC-PBE energy profile is free of the jumps that stem from hopping of the localized HF spin density between Ti sites. At least in this system, DC-PBE appears to offer an alternative means to achieve MP2-quality results at HF cost. PBE0 already affords accurate energetics (comparable to MP2) along the PBE, PBE0, and HSE06 optimization pathways, but DC-PBE0 shifts these energetics upward by 0.02–0.03 hartree. The use of DC-PBE0 therefore does not offer any advantage over PBE0 itself because both methods require the computational equivalent of a HF calculation.

Of the  $\sim 0.2$  hartree of energy lowering that is obtained at the PBE level when the HF-optimized starting structure is relaxed (Figure 6a), comparison to the DC-PBE result suggests that about half of that amount is density-driven error. In the PBE0 optimization, the difference between PBE and DC-PBE is much smaller, consistent with the idea that the density-driven error is reduced when a hybrid functional is used for the optimization. Shifts between DFT and DC-DFT are plotted in Figure S11 for two functionals and two optimization pathways, demonstrating that the shift for PBE0 is consistently smaller than that for PBE, as a result of the smaller density-driven error in the hybrid functional.

The optimization pathway obtained using the HSE06 functional<sup>94,95</sup> affords results that are very similar to PBE0-driven optimizations. This is not entirely surprising, given that HSE06 is a short-range hybrid designed to mimic PBE0 while reducing cost under periodic boundary conditions. The SCAN functional<sup>96</sup> affords energetics that are close to MP2 along various optimization pathways (Figure S12), but that means that DC-SCAN shifts the energies upward relative to MP2. The same is true for the hybrid SCAN0 functional.<sup>97</sup> The DC-SCAN procedure has been recommended in some recent work,<sup>43–45</sup> but in this particular application the quality of SCAN energetics is somewhat degraded by density correction.

In summary, we have implemented DC-DFT along with its analytic gradient in the Q-Chem program and have assessed this technique as a means to describe the electronic and

geometrical structure of model systems containing polaron defects. In Al-doped silica, where EPR measurements suggest that the dopant-induced hole is localized on a single oxygen atom, GGA functionals and hybrids such as B3LYP and PBE0 instead delocalize the hole over more than one oxygen atom. DC-DFT versions of these same functionals afford a localized hole and structural distortion that is consistent with experiment, i.e., a single elongated Al–O bond. This suggests that DC-DFT might be an alternative to hybrid functionals in these systems.

As a second application, we studied localization of an extra electron in a sizable cluster model of anatase TiO<sub>2</sub>. EPR spectroscopy of electron polarons in this system has certain features that are thought to be consistent with a localized Ti<sup>3+</sup> defect but has other features consistent with delocalization and a “large polaron”.<sup>73</sup> Starting from a HF-optimized structure with a localized polaron, we find that optimization with PBE0 or HSE06 preserves the defect localization whereas optimization with PBE drives delocalization onto multiple Ti atoms, leading to the elongation of multiple Ti–O bonds.

In both titania<sub>2</sub> and Al-doped silica, GGA-induced structural distortion is severe enough that a subsequent PBE0 single-point calculation cannot recover a localized polaron because exaggerated bond dipoles over multiple stretched bonds provide a driving force for delocalization and cause fractionation of the spin density. This is a significant observation insofar as a standard procedure in computational materials science is to perform structure relaxations using a GGA (often PBE) followed by single-point energy calculations with a hybrid functional (often PBE0 or HSE06). That procedure affords qualitatively incorrect electronic structure in several of the examples considered here.

For relaxation of the polaron in TiO<sub>2</sub>, DC-PBE affords energetics in good agreement with MP2. For the PBE0 and SCAN functionals, however, DC-DFT worsens what had been favorable agreement with the MP2 results. Because the cost of DC-DFT in periodic calculations will be similar to the cost of plain PBE0, we suggest that the role of DC-DFT should be a diagnostic one: where SIE problems are anticipated, DC-DFT provides an indication of whether defect delocalization is likely to persist as the fraction of exact exchange is adjusted. It does so without adjustable parameters and without the need to abandon electron correlation. The DC-DFT analytic gradient, missing in widely used quantum chemistry programs until now,<sup>41,42</sup> affords the ability to describe structural relaxation with this method and thus to interrogate how the elimination of SIE impacts the geometric structure of molecules and materials.

## ■ ASSOCIATED CONTENT

### SI Supporting Information

The Supporting Information is available free of charge at <https://pubs.acs.org/doi/10.1021/acs.jpcllett.2c01187>.

Computational details and additional analysis (PDF)

Transparent Peer Review report available (PDF)

## ■ AUTHOR INFORMATION

### Corresponding Author

John M. Herbert – Department of Chemistry and Biochemistry, The Ohio State University, Columbus, Ohio 43210, United States; [orcid.org/0000-0002-1663-2278](https://orcid.org/0000-0002-1663-2278); Email: [herbert@chemistry.ohio-state.edu](mailto:herbert@chemistry.ohio-state.edu)

## Authors

**Bhaskar Rana** – Department of Chemistry and Biochemistry, The Ohio State University, Columbus, Ohio 43210, United States; Present Address: Department of Chemistry, Stanford University, Stanford, California 94305, United States; [orcid.org/0000-0002-8751-7314](https://orcid.org/0000-0002-8751-7314)

**Marc P. Coons** – Department of Chemistry and Biochemistry, The Ohio State University, Columbus, Ohio 43210, United States; Present Address: The Dow Chemical Company, Midland, Michigan 48674, United States.; [orcid.org/0000-0001-9511-2854](https://orcid.org/0000-0001-9511-2854)

Complete contact information is available at:  
<https://pubs.acs.org/10.1021/acs.jpcllett.2c01187>

## Author Contributions

<sup>†</sup>B.R. and M.P.C. contributed equally to this work

## Notes

The authors declare the following competing financial interest(s): J.M.H. serves on the board of directors of Q-Chem Inc.

## ACKNOWLEDGMENTS

The authors thank Dr. Bushra Alam for assistance in constructing some of the cluster models. This work was supported by National Science Foundation grant nos. CHE-1665322 and CHE-1955282. Calculations were performed at the Ohio Supercomputer Center.<sup>98</sup>

## REFERENCES

- (1) Perdew, J. P.; Zunger, A. Self-interaction correction to density-functional approximations for many-electron systems. *Phys. Rev. B* **1981**, *23*, 5048–5079.
- (2) Perdew, J. P.; Ruzsinszky, A.; Sun, J.; Pederson, M. R. Paradox of self-interaction correction: How can anything so right be so wrong? *Adv. Atom. Mol. Opt. Phys.* **2015**, *64*, 1–14.
- (3) Cohen, A. J.; Mori-Sanchez, P.; Yang, W. Challenges for density functional theory. *Chem. Rev.* **2012**, *112*, 289–320.
- (4) Ruzsinszky, A.; Perdew, J. P.; Csonka, G. I.; Vydrov, O. A.; Scuseria, G. E. Spurious fractional charge of dissociated atoms: Pervasive and resilient self-interaction error of common density functionals. *J. Chem. Phys.* **2006**, *125*, 194112.
- (5) Lynch, B. J.; Truhlar, D. G. How well can hybrid density functional methods predict transition state geometries and barrier heights? *J. Phys. Chem. A* **2001**, *105*, 2936–2941.
- (6) Janesko, B. Replacing hybrid density functional theory: Motivation and recent advances. *Chem. Soc. Rev.* **2021**, *50*, 8470–8495.
- (7) Braïda, B.; Hiberty, P. C.; Savin, A. A systematic failing of current density functionals: Overestimation of two-center three-electron bonding energies. *J. Phys. Chem. A* **1998**, *102*, 7872–7877.
- (8) Sodupe, M.; Bertran, J.; Rodríguez-Santiago, L.; Baerends, E. J. Ground state of the  $(\text{H}_2\text{O})_2^+$  radical cation: DFT versus post-Hartree-Fock methods. *J. Phys. Chem. A* **1999**, *103*, 166–170.
- (9) Herbert, J. M.; Head-Gordon, M. Calculation of electron detachment energies for water cluster anions: An appraisal of electronic structure methods, with application to  $(\text{H}_2\text{O})_{20}^-$  and  $(\text{H}_2\text{O})_{24}^-$ . *J. Phys. Chem. A* **2005**, *109*, 5217–5229.
- (10) Mantz, Y. A.; Gervasio, F. L.; Laino, T.; Parrinello, M. Charge localization in stacked radical cation DNA base pairs and the benzene dimer studied by self-interaction corrected density-functional theory. *J. Phys. Chem. A* **2007**, *111*, 105–112.
- (11) Livshits, E.; Granot, R. S.; Baer, R. A density functional theory for studying ionization processes in water clusters. *J. Phys. Chem. A* **2011**, *115*, 5735–5744.
- (12) Tentscher, P. R.; Arey, J. S. Binding in radical-solvent binary complexes: Benchmark energies and performance of approximate methods. *J. Chem. Theory Comput.* **2013**, *9*, 1568–1579.
- (13) Johnson, E. R.; Salamone, M.; Bietti, M.; DiLabio, G. A. Modeling noncovalent radical-molecule interactions using conventional density-functional theory: Beware erroneous charge transfer. *J. Phys. Chem. A* **2013**, *117*, 947–952.
- (14) Kim, M.-C.; Sim, E.; Burke, K. Ions in solution: Density corrected density functional theory (DC-DFT). *J. Chem. Phys.* **2014**, *140*, 18A528.
- (15) Kim, M.-C.; Park, H.; Son, S.; Sim, E.; Burke, K. Improved DFT potential energy surfaces via improved densities. *J. Phys. Chem. Lett.* **2015**, *6*, 3802–3807.
- (16) VandeVondele, J.; Sprik, M. A molecular dynamics study of the hydroxyl radical in solution applying self-interaction-corrected density functional methods. *Phys. Chem. Chem. Phys.* **2005**, *7*, 1363–1367.
- (17) Rana, B.; Herbert, J. M. Role of hemibonding in the structure and ultraviolet spectroscopy of the aqueous hydroxyl radical. *Phys. Chem. Chem. Phys.* **2020**, *22*, 27829–27844.
- (18) Rana, B.; Herbert, J. M. Hidden hemibonding in the aqueous hydroxyl radical. *J. Phys. Chem. Lett.* **2021**, *12*, 8053–8060.
- (19) Sai, N.; Barbara, P. F.; Leung, K. Hole localization in molecular crystals from hybrid density functional theory. *Phys. Rev. Lett.* **2011**, *106*, 226403.
- (20) Lany, S. Predicting polaronic defect states by means of generalized Koopmans density functional calculations. *Phys. Status Solidi B* **2011**, *248*, 1052–1060.
- (21) Ansari, N.; Ulman, K.; Camellone, M. F.; Seriani, N.; Gebauer, R.; Piccinin, S. Hole localization in  $\text{Fe}_2\text{O}_3$  from density functional theory and wave-function-based methods. *Phys. Rev. Mater.* **2017**, *1*, 035404.
- (22) To, J.; Sokol, A. A.; French, S. A.; Kaltsoyannis, N.; Catlow, C. R. A. Hole localization in  $[\text{AlO}_4]^0$  defects in silica materials. *J. Chem. Phys.* **2005**, *122*, 144704.
- (23) Lægsgaard, J.; Stokbro, K. Hole trapping at Al impurities in silica: A challenge for density functional theories. *Phys. Rev. Lett.* **2001**, *86*, 2834–2837.
- (24) Gerosa, M.; Di Valentin, C.; Bottani, C. E.; Onida, G.; Pacchion, G. Hole localization in Al-doped quartz  $\text{SiO}_2$  within *ab initio* hybrid-functional DFT. *J. Chem. Phys.* **2015**, *143*, 111103.
- (25) Laegsgaard, J.; Stokbro, K. Electronic structure and hyperfine parameters of substitutional Al and P impurities in silica. *Phys. Rev. B* **2002**, *65*, 107520.
- (26) Gillen, R.; Robertson, J. Hybrid functional calculations of the Al impurity in  $\alpha$  quartz: Hole localization and electron paramagnetic resonance parameters. *Phys. Rev. B* **2012**, *85*, 014117.
- (27) Pacchioni, G.; Frigoli, F.; Ricci, D.; Weil, J. A. Theoretical description of hole localization in a quartz Al center: The importance of exact electron exchange. *Phys. Rev. B* **2000**, *63*, 054102.
- (28) d’Avezac, M.; Calandra, M.; Mauri, F. Density functional theory description of hole-trapping in  $\text{SiO}_2$ : A self-interaction-corrected approach. *Phys. Rev. B* **2005**, *71*, 205210.
- (29) Zawadzki, P.; Rossmeisl, J.; Jacobsen, K. W. Electronic hole transfer in rutile and anatase  $\text{TiO}_2$ : Effect of a delocalization error in the density functional theory on the charge transfer barrier height. *Phys. Rev. B* **2011**, *84*, 121203.
- (30) Spreafico, C.; VandeVondele, J. The nature of excess electrons in anatase and rutile from hybrid DFT and RPA. *Phys. Chem. Chem. Phys.* **2014**, *16*, 26144–26152.
- (31) Elmaslmane, A. R.; Watkins, M. B.; McKenna, K. P. First-principles modeling of polaron formation in  $\text{TiO}_2$  polymorphs. *J. Chem. Theory Comput.* **2018**, *14*, 3740–3751.
- (32) Liu, T.; Cui, M.; Dupuis, M. Hole polaron transport in bismuth vanadate  $\text{BiVO}_4$  from hybrid density functional theory. *J. Phys. Chem. C* **2020**, *124*, 23038–23044.
- (33) Verma, P.; Perera, A.; Bartlett, R. J. Increasing the applicability of DFT I: Non-variational correlation corrections from Hartree-Fock DFT for predicting transition states. *Chem. Phys. Lett.* **2012**, *524*, 10–15.

- (34) Janesko, B. G.; Scuseria, G. E. Hartree-Fock orbitals significantly improve the reaction barrier heights predicted by semilocal density functionals. *J. Chem. Phys.* **2008**, *128*, 244112.
- (35) Gill, P. M. W.; Johnson, B. G.; Pople, J. A.; Frisch, M. J. An investigation of the performance of a hybrid of Hartree-Fock and density functional theory. *Int. J. Quantum Chem. Symp.* **1992**, *44*, 319–331.
- (36) Oliphant, N.; Bartlett, R. A systematic comparison of molecular properties obtained using Hartree-Fock, a hybrid Hartree-Fock density-functional-theory, and coupled-cluster methods. *J. Chem. Phys.* **1994**, *100*, 6550–6561.
- (37) Kim, M.-C.; Sim, E.; Burke, K. Understanding and reducing errors in density functional calculations. *Phys. Rev. Lett.* **2013**, *111*, 073003.
- (38) Vuckovic, S.; Song, S.; Kozłowski, J.; Sim, E.; Burke, K. Density functional analysis: The theory of density-corrected DFT. *J. Chem. Theory Comput.* **2019**, *15*, 6636–6646.
- (39) Sim, E.; Song, S.; Burke, K. Quantifying density errors in DFT. *J. Phys. Chem. Lett.* **2018**, *9*, 6385–6392.
- (40) Song, S.; Vuckovic, S.; Sim, E.; Burke, K. Density sensitivity of empirical functionals. *J. Phys. Chem. Lett.* **2021**, *12*, 800–807.
- (41) Song, S.; Vuckovic, S.; Sim, E.; Burke, K. Density corrected DFT explained: Questions and answers. *J. Chem. Theory Comput.* **2022**, *18*, 817–827.
- (42) Sim, E.; Song, S.; Vuckovic, S.; Burke, K. Improving results by improving densities: Density-corrected density functional theory. *J. Am. Chem. Soc.* **2022**, *144*, 6625–6639.
- (43) Dasgupta, S.; Lambros, E.; Perdew, J. P.; Paesani, F. Elevating density functional theory to chemical accuracy for water simulations through a density-corrected many-body formalism. *Nat. Commun.* **2021**, *12*, 6359.
- (44) Palos, E.; Lambros, E.; Swee, S.; Hu, J.; Dasgupta, S.; Paesani, F. Assessing the interplay between functional-driven and density-driven errors in DFT models of water. *J. Chem. Theory Comput.* **2022**, DOI: 10.1021/acs.jctc.2c00050.
- (45) Dasgupta, S.; Shahi, C.; Bhetwal, P.; Perdew, J. P.; Paesani, F. How good is the density-corrected SCAN functional for neutral and ionic aqueous systems, and what is so right about the Hartree-Fock density? DOI: 10.26434/chemrxiv-2022-8r5v9.
- (46) Santra, G.; Martin, J. M. L. What types of chemical problems benefit from density-corrected DFT? A probe using an extensive and chemically diverse test suite. *J. Chem. Theory Comput.* **2021**, *17*, 1368–1379.
- (47) Schirmer, O. F.  $O^-$  bound small polarons in oxide materials. *J. Phys.: Condens. Matter* **2006**, *18*, R667–R704.
- (48) Rettie, A. J. E.; Chemelewski, W. D.; Emin, D.; Mullins, C. B. Unravelling small-polaron transport in metal oxide photoelectrodes. *J. Phys. Chem. Lett.* **2016**, *7*, 471–479.
- (49) Strand, J.; Kaviani, M.; Gao, D.; El-Sayed, A.-M.; Afanas'ev, V. V.; Shluger, A. L. Intrinsic charge trapping in amorphous oxide films: Status and challenges. *J. Phys.: Condens. Matter* **2018**, *30*, 233001.
- (50) Biswas, S.; Husek, J.; Londo, S.; Baker, L. R. Highly localized charge transfer excitons in metal oxide semiconductors. *Nano Lett.* **2018**, *18*, 1228–1233.
- (51) Bandaranayake, S.; Hruska, E.; Londo, S.; Biswas, S.; Baker, L. R. Small polarons and surface defects in metal oxide photocatalysts studied using XUV reflection-absorption spectroscopy. *J. Phys. Chem. C* **2020**, *124*, 22853–22870.
- (52) Shluger, A. L.; McKenna, K. P.; Sushko, P. V.; Muñoz-Ramo, D.; Kimmel, A. V. Modelling of electron and hole trapping in oxides. *Modelling Simul. Mater. Sci. Eng.* **2009**, *17*, 084004.
- (53) Handy, N. C.; Schaefer, H. F., III On the evaluation of analytic energy derivatives for correlated wave functions. *J. Chem. Phys.* **1984**, *81*, 5031–5033.
- (54) Pople, J. A.; Krishnan, R.; Schlegel, H. B.; Binkley, J. S. Derivative studies in Hartree-Fock and Møller-Plesset theories. *Int. J. Quantum Chem.* **1979**, *13*, 225–241.
- (55) Handy, N. C.; Tozer, D. J.; Laming, G. J.; Murray, C. W.; Amos, R. D. Analytic second derivatives of the potential energy surface. *Isr. J. Chem.* **1993**, *33*, 331–344.
- (56) Johnson, B. G.; Fisch, M. J. An implementation of analytic second derivatives of the gradient-corrected density functional energy. *J. Chem. Phys.* **1994**, *100*, 7429–7442.
- (57) Anderson, L. N.; Oviedo, M. B.; Wong, B. M. Accurate electron affinities and orbital energies of anions from a nonempirically tuned range-separated density functional theory approach. *J. Chem. Theory Comput.* **2017**, *13*, 1656–1666.
- (58) Gauss, J. Molecular Properties. In *Modern Methods and Algorithms of Quantum Chemistry*, 2nd ed.; Grotendorst, J., Ed.; NIC Series; John von Neumann Institute for Computing: Jülich, 2000; Vol. 3, pp 541–592.
- (59) Epifanovsky, E.; Gilbert, A. T. B.; Feng, X.; Lee, J.; Mao, Y.; Mardirossian, N.; Pokhilko, P.; White, A. F.; Coons, M. P.; Dempwolff, A. L.; Gan, Z.; Hait, D.; Horn, P. R.; Jacobson, L. D.; Kaliman, I.; Kussmann, J.; Lange, A. W.; Lao, K. U.; Levine, D. S.; Liu, J.; McKenzie, S. C.; Morrison, A. F.; Nanda, K. D.; Plasser, F.; Rehn, D. R.; Vidal, M. L.; You, Z.-Q.; Zhu, Y.; Alam, B.; Albrecht, B. J.; Aldossary, A.; Alguire, E.; Andersen, J. H.; Athavale, V.; Barton, D.; Begam, K.; Behn, A.; Bellonzi, N.; Bernard, Y. A.; Berquist, E. J.; Burton, H. G. A.; Carreras, A.; Carter-Fenk, K.; Chakraborty, R.; Chien, A. D.; Closser, K. D.; Cofer-Shabica, V.; Dasgupta, S.; de Wergifosse, M.; Deng, J.; Diedenhofen, M.; Do, H.; Ehlert, S.; Fang, P.-T.; Fatehi, S.; Feng, Q.; Friedhoff, T.; Gayvert, J.; Ge, Q.; Gidofalvi, G.; Goldey, M.; Gomes, J.; González-Espinoza, C. E.; Gulania, S.; Gunina, A. O.; Hanson-Heine, M. W. D.; Harbach, P. H. P.; Hauser, A.; Herbst, M. F.; Hernández Vera, M.; Hodecker, M.; Holden, Z. C.; Houck, S.; Huang, X.; Hui, K.; Huynh, B. C.; Ivanov, M.; Jász, A.; Ji, H.; Jiang, H.; Kaduk, B.; Kähler, S.; Khistyayev, K.; Kim, J.; Kis, G.; Klunzinger, P.; Koczor-Benda, Z.; Koh, J. H.; Kosenkov, D.; Koulias, L.; Kowalczyk, T.; Krauter, C. M.; Kue, K.; Kunitsa, A.; Kus, T.; Ladžanski, I.; Landau, A.; Lawler, K. V.; Lefrançois, D.; Lehtola, S.; Li, R. R.; Li, Y.-P.; Liang, J.; Liebenthal, M.; Lin, H.-H.; Lin, Y.-S.; Liu, F.; Liu, K.-Y.; Loipersberger, M.; Luenser, A.; Manjanath, A.; Manohar, P.; Mansoor, E.; Manzer, S. F.; Mao, S.-P.; Marenich, A. V.; Markovich, T.; Mason, S.; Maurer, S. A.; McLaughlin, P. F.; Menger, M. F. S. J.; Mewes, J.-M.; Mewes, S. S.; Morgante, P.; Mullinax, J. W.; Oosterbaan, K. J.; Paran, G.; Paul, A. C.; Paul, S. K.; Pavošević, F.; Pei, Z.; Prager, S.; Proynov, E. I.; Rák, A.; Ramos-Cordoba, E.; Rana, B.; Rask, A. E.; Rettig, A.; Richard, R. M.; Rob, F.; Rossomme, E.; Scheele, T.; Scheurer, M.; Schneider, M.; Sergueev, N.; Sharada, S. M.; Skomorowski, W.; Small, D. W.; Stein, C. J.; Su, Y.-C.; Sundstrom, E. J.; Tao, Z.; Thirman, J.; Tornai, G. J.; Tsuchimochi, T.; Tubman, N. M.; Veccham, S. P.; Vydrov, O.; Wenzel, J.; Witte, J.; Yamada, A.; Yao, K.; Yeganeh, S.; Yost, S. R.; Zech, A.; Zhang, I. Y.; Zhang, X.; Zhang, Y.; Zuev, D.; Aspuru-Guzik, A.; Bell, A. T.; Besley, N. A.; Bravaya, K. B.; Brooks, B. R.; Casanova, D.; Chai, J.-D.; Coriani, S.; Cramer, C. J.; Cserey, G.; DePrince, A. E., III; DiStasio, R. A., Jr.; Dreuw, A.; Dunietz, B. D.; Furlani, T. R.; Goddard, A., III; Hammes-Schiffer, S.; Head-Gordon, T.; Hehre, W. J.; Hsu, C.-P.; Jagau, T.-C.; Jung, Y.; Klamt, A.; Kong, J.; Lambrecht, D. S.; Liang, W.; Mayhall, N. J.; McCurdy, C. W.; Neaton, J. B.; Ochsenfeld, C.; Parkhill, J. A.; Peverati, R.; Rassolov, V. A.; Shao, Y.; Slipchenko, L. V.; Stauch, T.; Steele, R. P.; Subotnik, J. E.; Thom, A. J. W.; Tkatchenko, A.; Truhlar, D. G.; van Voorhis, T.; Wesolowski, T. A.; Whaley, K. B.; Woodcock, H. L., III; Zimmerman, P. M.; Faraji, S.; Gill, P. M. W.; Head-Gordon, M.; Herbert, J. M.; Krylov, A. I. Software for the frontiers of quantum chemistry: An overview of developments in the Q-Chem 5 package. *J. Chem. Phys.* **2021**, *155*, 084801.
- (60) Lægsgaard, J.; Stokbro, K. Local chemistry of Al and P impurities in silica. *Phys. Rev. B* **2000**, *61*, 12590–12593.
- (61) Nolan, M.; Watson, G. W. The electronic structure of alkali doped alkaline earth metal oxides: Li doping of MgO studied with DFT-GGA and GGA+U. *Surf. Sci.* **2005**, *586*, 25–37.
- (62) Nolan, M.; Watson, G. W. Hole localization in Al doped silica: a DFT + U description. *J. Chem. Phys.* **2006**, *125*, 144701.

- (63) Liao, P.; Carter, E. A. Hole transport in pure and doped hematite. *J. Appl. Phys.* **2012**, *112*, 013701.
- (64) Schnadt, R.; Rauber, A. Motional effects in the trapped-hole center in smoky quartz. *Solid State Commun.* **1971**, *9*, 159–161.
- (65) Nuttall, R. H. D.; Weil, J. A. Oxygen-17 hyperfine structure of trapped-hole center  $[\text{AlO}_4]^0$  in  $\alpha$ -quartz. *Solid State Commun.* **1980**, *35*, 789–791.
- (66) Nuttall, R. H. D.; Weil, J. A. The magnetic properties of the oxygen-hole aluminum centers in crystalline  $\text{SiO}_2$ . I.  $[\text{AlO}_4]^0$ . *Can. J. Phys.* **1981**, *59*, 1696–1708.
- (67) Di Valentin, C.; Pacchioni, G.; Selloni, A. Electronic structure of defect states in hydroxylated and reduced rutile  $\text{TiO}_2$  surfaces. *Phys. Rev. Lett.* **2006**, *97*, 166803.
- (68) Di Valentin, C.; Selloni, A. Bulk and surface polarons in photoexcited anatase  $\text{TiO}_2$ . *J. Phys. Chem. Lett.* **2011**, *2*, 2223–2228.
- (69) Linsebigler, A. L.; Lu, G.; Yates, J. T., Jr. Photocatalysis on  $\text{TiO}_2$  surfaces: Principles, mechanisms, and selected results. *Chem. Rev.* **1995**, *95*, 735–758.
- (70) Hadjiivanov, K. I.; Klissurski, D. G. Surface chemistry of titania (anatase) and titania-supported catalysts. *Chem. Soc. Rev.* **1996**, *25*, 61–69.
- (71) Hagfeldt, A.; Boschloo, G.; Sun, L.; Kloo, L.; Pettersson, H. Dye-sensitized solar cells. *Chem. Rev.* **2010**, *110*, 6595–6663.
- (72) Bai, Y.; Mora-Seró, I.; de Angelis, F.; Bisquert, J.; Wang, P. Titanium dioxide nanomaterials for photovoltaic applications. *Chem. Rev.* **2014**, *114*, 10095–10130.
- (73) Livraghi, S.; Chiesa, M.; Paganini, M. C.; Giamello, E. On the nature of reduced states in titanium dioxide as monitored by electron paramagnetic resonance. I: The anatase case. *J. Phys. Chem. C* **2011**, *115*, 25413–25421.
- (74) Setvin, J. M.; Franchini, C.; Hao, X.; Schmid, M.; Janotti, A.; Kaltak, M.; de Walle, C. G. V.; Kresse, G.; Diebold, U. Direct view at excess electrons in  $\text{TiO}_2$  rutile and anatase. *Phys. Rev. Lett.* **2014**, *113*, 086402.
- (75) De Lile, J. R.; Kang, S. G.; Son, Y.-A.; Lee, S. G. Investigating polaron formation in anatase and brookite  $\text{TiO}_2$  by density functional theory with hybrid-functional and DFT +  $U$  methods. *ACS Omega* **2019**, *4*, 8056–8064.
- (76) Di Valentin, C.; Pacchioni, G.; Selloni, A. Reduced and n-type doped  $\text{TiO}_2$ : Nature of  $\text{Ti}^{3+}$  species. *J. Phys. Chem. C* **2009**, *113*, 20543–20552.
- (77) Finazzi, E.; Di Valentin, C.; Pacchioni, G.; Selloni, A. Excess electron states in reduced bulk anatase  $\text{TiO}_2$ : Comparison of standard GGA, GGA +  $U$ , and hybrid DFT calculations. *J. Chem. Phys.* **2008**, *129*, 154113.
- (78) Deskins, N. A.; Rousseau, R.; Dupuis, M. Localized electronic states from surface hydroxyls and polarons in  $\text{TiO}_2(110)$ . *J. Phys. Chem. C* **2009**, *113*, 14583–14586. Erratum: *J. Phys. Chem. C* **2014**, *118*, 13326–13327.
- (79) Deskins, N. A.; Rousseau, R.; Dupuis, M. Distribution of  $\text{Ti}^{3+}$  surface sites in reduced  $\text{TiO}_2$ . *J. Phys. Chem. C* **2011**, *115*, 7562–7572. Erratum: *J. Phys. Chem. C* **2014**, *118*, 13326–13327.
- (80) Zhao, Q.; Kulik, H. J. Where does the density localize in the solid state? Divergent behavior for hybrids and DFT+ $U$ . *J. Chem. Theory Comput.* **2018**, *14*, 670–683.
- (81) Blagojevic, V.; Chen, Y.-R.; Steigerwald, M.; Brus, L.; Friesner, R. A. Quantum chemical investigation of cluster models for  $\text{TiO}_2$  nanoparticles with water-derived ligand passivation: Studies of excess electron states and implications for charge transport in the Gratzel cell. *J. Phys. Chem. C* **2009**, *113*, 19806–19811.
- (82) Hay, P. J.; Wadt, W. R. *Ab initio* effective core potentials for molecular calculations. Potentials for K to Au including the outermost core orbitals. *J. Chem. Phys.* **1985**, *82*, 299–310.
- (83) Pham, T. D.; Deskins, N. A. Efficient method for modeling polarons using electronic structure methods. *J. Chem. Theory Comput.* **2020**, *16*, 5264–5278.
- (84) Shibuya, T.; Yasuoka, K.; Mirbt, S.; Sanyal, B. A systematic study of polarons due to oxygen vacancy formation at the rutile  $\text{TiO}_2(110)$  surface by GGA +  $U$  and HSE06 methods. *J. Phys.: Condens. Matter* **2012**, *24*, 435504.
- (85) Zhang, Y.; Yang, W. A challenge for density functionals: Self-interaction error increases for systems with a noninteger number of electrons. *J. Chem. Phys.* **1998**, *109*, 2604–2608.
- (86) Hamad, S.; Catlow, C. R. A.; Woodley, S. M.; Lago, S.; Majías, J. A. Structure and stability of small  $\text{TiO}_2$  nanoparticles. *J. Phys. Chem. B* **2005**, *109*, 15741–15748.
- (87) Onal, I.; Soyer, S.; Senkan, S. Adsorption of water and ammonia on  $\text{TiO}_2$ -anatase cluster models. *Surf. Sci.* **2006**, *600*, 2457–2469.
- (88) Yang, L.; Taylor, R.; de Jong, W. A.; Hase, W. L. A model DMMP/ $\text{TiO}_2(110)$  intermolecular potential energy function developed from ab initio calculations. *J. Phys. Chem. C* **2011**, *115*, 12403–12413.
- (89) Chen, M.; Straatsma, T. P.; Dixon, D. A. Molecular and dissociative adsorption of water on  $(\text{TiO}_2)_n$  clusters,  $n = 1-4$ . *J. Phys. Chem. A* **2015**, *119*, 11406–11421.
- (90) Wang, H.; Ji, Y.; Chen, J.; Li, G.; An, T. Theoretical investigation on the adsorption configuration and  $\cdot\text{OH}$ -initiated photocatalytic degradation mechanism of typical atmospheric VOCs styrene onto  $(\text{TiO}_2)_n$  clusters. *Sci. Rep.* **2015**, *5*, 15059.
- (91) Capelle, K. A bird's-eye view of density-functional theory. *Braz. J. Phys.* **2006**, *36*, 1318–1343.
- (92) Mori-Sánchez, P.; Cohen, A. J.; Yang, W. Localization and delocalization errors in density functional theory and implications for band-gap prediction. *Phys. Rev. Lett.* **2008**, *100*, 146401.
- (93) Perdew, J. P.; Yang, W.; Burke, K.; Yang, Z.; Gross, E. K. U.; Scheffler, M.; Scuseria, G. E.; Henderson, T. M.; Zhang, I. Y.; Ruzsinszky, A.; Peng, H.; Sun, J.; Trushin, E.; Görling, A. Understanding band gaps of solids in generalized Kohn-Sham theory. *Proc. Natl. Acad. Sci. U.S.A.* **2017**, *114*, 2801–2806.
- (94) Heyd, J.; Scuseria, G. E.; Ernzerhof, M. Hybrid functionals based on a screened Coulomb potential. *J. Chem. Phys.* **2003**, *118*, 8207–8215. Erratum: *J. Chem. Phys.* **2006**, *124*, 219906.
- (95) Krukau, A. V.; Vydrov, O. A.; Izmaylov, A. F.; Scuseria, G. E. Influence of the exchange screening parameter on the performance of screened hybrid functionals. *J. Chem. Phys.* **2006**, *125*, 224106.
- (96) Sun, J.; Ruzsinszky, A.; Perdew, J. P. Strongly constrained and appropriately normed semilocal density functional. *Phys. Rev. Lett.* **2015**, *115*, 036402.
- (97) Hui, K.; Chai, J.-D. SCAN-based hybrid and double-hybrid density functionals from models without fitted parameters. *J. Chem. Phys.* **2016**, *144*, 044114.
- (98) Ohio Supercomputer Center, <http://osc.edu/ark:/19495/f5s1ph73>.